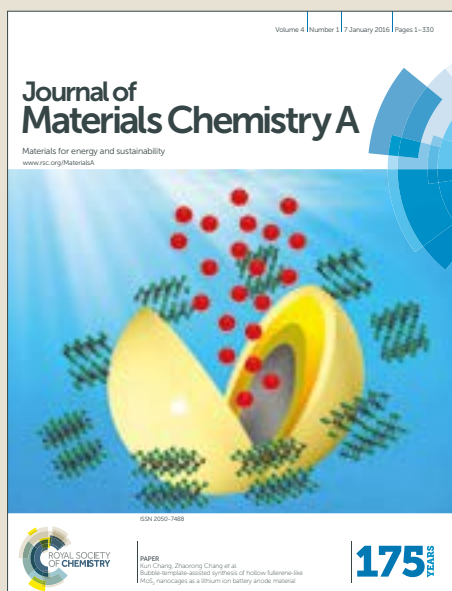


Journal of Materials Chemistry A

Accepted Manuscript



This article can be cited before page numbers have been issued, to do this please use: J. Xie, H. Qu, F. Lei, X. Peng, W. Liu, L. Gao, P. Hao, G. Cui and B. Tang, *J. Mater. Chem. A*, 2018, DOI: 10.1039/C8TA05054F.



This is an Accepted Manuscript, which has been through the Royal Society of Chemistry peer review process and has been accepted for publication.

Accepted Manuscripts are published online shortly after acceptance, before technical editing, formatting and proof reading. Using this free service, authors can make their results available to the community, in citable form, before we publish the edited article. We will replace this Accepted Manuscript with the edited and formatted Advance Article as soon as it is available.

You can find more information about Accepted Manuscripts in the [author guidelines](#).

Please note that technical editing may introduce minor changes to the text and/or graphics, which may alter content. The journal's standard [Terms & Conditions](#) and the ethical guidelines, outlined in our [author and reviewer resource centre](#), still apply. In no event shall the Royal Society of Chemistry be held responsible for any errors or omissions in this Accepted Manuscript or any consequences arising from the use of any information it contains.



Journal Name

ARTICLE

Partially Amorphous Nickel-Iron Layered Double Hydroxide Nanosheet Arrays for Robust Bifunctional Electrocatalysis

Junfeng Xie,^{a,†,*} Haichao Qu,^{a,†} Fengcai Lei,^a Xu Peng,^b Weiwei Liu,^a Li Gao,^a Pin Hao,^a Guanwei Cui,^a Bo Tang^{a,*}

Received 00th January 20xx,
Accepted 00th January 20xx

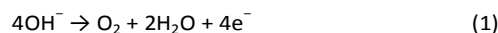
DOI: 10.1039/x0xx00000x

www.rsc.org/

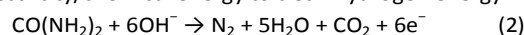
Bifunctional electrocatalysts that can boost energy-related reactions are urgently demanded to pursue dual and even multiple targets towards practical applications such as energy conversion, clean fuel production and pollution treatment. Herein, we highlight that in-situ grown nickel-iron layered double hydroxide (NiFe LDH) nanosheet array catalyst with partially amorphous characteristics, rich native Ni³⁺ ions and optimal Ni:Fe ratio can exhibit robust performances on both oxygen evolution reaction (OER) and urea oxidation reaction (UOR). Benefited from the partially amorphous feature, the catalytically active high-valence species are easy to be generated and stabilized, thus further realizing enhanced electrooxidation activity with the aid of the internal 2D charge transfer pathway and native Ni³⁺ ions. As expected, the partially amorphous catalyst exhibits a higher OER current of 284.4 mA cm⁻² at an overpotential of 500 mV, which shows 2.2~10.0 times enhancement than the counterparts with various Ni:Fe ratios. In addition, the UOR current density of the partially amorphous catalyst at 1.8 V vs. RHE shows 1.6 and 2.4 times increment relative to fully amorphous and highly crystalline catalysts, and 2.7-9.4 folds larger than the catalysts with other Ni:Fe ratios. The optimization strategy of designing partially amorphous bifunctional catalyst in this work may broaden the way on searching for advanced electrocatalysts for simultaneous waste water treatment and clean energy production.

Introduction

Electrocatalytic energy conversion has attracted extensive attention owing to its multiple benefits such as high efficiency, good reaction selectivity combined with environmentally benign morality.^{1, 2} Among a large variety of the electrocatalytic pathways, electrocatalytic oxygen evolution reaction (OER) for water electrolysis and electrooxidation of energy-containing small molecules like urea are highly attractive. On the one hand, OER has not only been regarded as an important process for overall water splitting and co-catalysis in photoelectrochemical reactions but also as the rate-limiting half reaction in water electrolysis owing to its sluggish 4-electron reaction mechanism (equation 1):^{3, 4}



On the other hand, urea, as a common waste in polluted water, has been considered to be a promising chemical for hydrogen generation in electrolyzer cells.⁵ During the electrocatalytic urea oxidation reaction (UOR) in alkaline media, N₂ and CO₂ are generated from the anode, while water can be reduced at the cathode to produce hydrogen via HER.⁶ Of note, the equilibrium potential of the electrochemical UOR is only 0.37 V vs. RHE, which is much lower than the equilibrium potential of the OER (1.23 V vs. RHE).⁷ Therefore, UOR is in principle a more efficient process for producing hydrogen via coupled cathodic “water splitting”. Therefore, as a combined process for both energy conversion and pollution treatment, UOR also holds substantial research interests, while unfortunately few catalysts are explored owing to the harsh reaction mechanism which involves 6-electron transfer process (equation 2).^{5, 8-10} Of note, as the anodic reaction, either OER or UOR, can be coupled with the cathodic hydrogen evolution reaction (HER, equation 3) to realize the energy conversion from electricity/chemical energy to clean hydrogen energy.¹⁰⁻¹³



Based on this understanding and considering the variable urea concentration in industrial and sanitary waste water, exploring bifunctional OER/UOR electrocatalysts is urgently demanded,

^a College of Chemistry, Chemical Engineering and Materials Science, Key Laboratory of Molecular and Nano Probes (Ministry of Education), Collaborative Innovation Center of Functionalized Probes for Chemical Imaging in Universities of Shandong, Institute of Molecular and Nano Science, Shandong Normal University, Jinan, Shandong, 250014, P. R. China. E-mail: xiejf@sdu.edu.cn; tangb@sdu.edu.cn.

^b Hubei Collaborative Innovation Center for Advanced Organic Chemical Materials, Ministry-of-Education Key Laboratory for the Synthesis and Application of Organic Functional Molecules, College of Chemistry and Chemical Engineering, Hubei University, Wuhan, Hubei, 430062, P. R. China.

† J.X. and H.Q. contributed equally to this work.

Electronic Supplementary Information (ESI) available: Additional physical and electrochemical characterizations of catalysts with various crystallinity and Ni:Fe ratio. See DOI: 10.1039/x0xx00000x

ARTICLE

Journal Name

which can be directly used in electrochemical pollution treatment of urea-containing waste water and synergistically realize water splitting, while unfortunately few such catalysts are developed up to date.

Recently, oxygen-evolving electrocatalysts based on nickel-iron compounds have been widely studied benefited from their high Earth abundance, low cost and relatively high activity.¹⁴⁻²⁰ Both theoretical and experimental results have confirmed that Ni:Fe ratio is crucial in regulating the OER activity, and a pre-oxidation process of Ni²⁺ species is considered to be the prerequisite to catalyze OER, which is required to generate the catalytically active high-valence materials, commonly in the form of Fe:NiOOH, where the valence of nickel is from +3 to +4,²¹⁻²³ while as another electrooxidation reaction, the active sites of UOR are also suggested to be located at Ni³⁺ ions,⁸ and therefore increasing the intrinsic Ni³⁺ concentration or realizing facile generation of these high-valence species is also of great importance in optimizing the UOR activity. In addition, understanding the role of Ni:Fe ratio in UOR catalysis is also meaningful in guiding future designing of NiFe-based UOR catalysts. Towards the engineering of catalytically active species, constructing amorphous structure is usually considered to be an effective method to increase the active site generation of OER catalysts, in particular, NiFe-based materials,²⁴⁻²⁸ while the negative influence in decreasing the intrinsic conductivity is worthy to be particularly noted. In this case, modulating the crystallinity to fabricate partially amorphous structure would be a promising strategy in enhancing the electrooxidation performances, which could achieve an optimal balance between active sites and conductivity. In this work, by means of in-situ growing nickel-iron layered double hydroxide (NiFe LDH) nanosheet arrays on NiFe alloy foam, a self-supported anode with partially amorphous feature is fabricated, realizing robust performance towards OER and UOR catalysis. The partially amorphous nanosheets can not only provide abundant reactive sites for the electrochemical generation of high-valence species, but also result in rich crystalline-amorphous interfaces to form and stabilize native Ni³⁺ ions. Furthermore, the highly porous and conductive alloy skeleton accompanied by the nanosheet sub-units with high surface area and 2D charge transfer pathway further accelerate the electrocatalytic rate, and finally resulting in excellent OER and UOR activities.

Experimental

Materials

The nickel foam, iron foam and the alloyed NiFe foams were purchased from Suzhou Jiashide Co., Ltd. and the other reagents were purchased from Sinopharm Chemical Reagent Co., Ltd.. All chemicals were used as received unless noted specially.

Preparation of pa-NiFe LDH NS/NIF

Typically, 0.02 mmol urea was dissolved in 80 mL deionized water and stirred for 10 min to form a clear solution. Then, a piece of NiFe alloy foam (Ni:Fe ratio 1:5, denoted as NiFe₅ alloy foam, 1 cm×2 cm×1 mm) was treated by ultrasound in acetone for 5 min, then dry naturally at room temperature. The alloy foam was then immersed in 1% HCl solution, and once the bubble appeared the foam was allowed to be washed by deionized water immediately to ensure the removal of surface oxide and avoid obvious corrosion of the metallic skeleton. After that, the clean alloy foam was placed in Teflon-lined stainless steel autoclave and the urea solution was added. The reaction system was maintained at 100 °C for 12 hours, and then cooled down to room temperature naturally. The as-obtained black foam electrode was rinsed with distilled water and ethanol for several times and finally dried in vacuum at 60 °C overnight.

Modulation of crystallinity

In order to obtain fully amorphous NiFeO_x film on NiFe alloy foam (a-NiFeO_x/NIF) and highly crystalline NiFe LDH nanoplates on NiFe alloy foam (c-NiFe LDH NP/NIF), the synthesis temperatures were modulated as 80 °C and 140 °C, respectively, and other operations are the same as the synthesis process of pa-NiFe LDH NS/NIF.

Preparation of NiFe₂O₄ NP/NIF, Ni(OH)₂/NF and γ-Fe₂O₃/IF

By replacing the NiFe₅ alloy foam as NiFe_{7.7} alloy foam, pure Ni foam, pure Fe foam and keeping other operations unchanged, NiFe₂O₄ nanoplates grown on NiFe foam (NiFe₂O₄ NP/NIF), Ni(OH)₂ nanosheets grown on nickel foam (Ni(OH)₂/NF) as well as γ-Fe₂O₃ grown on iron foam (γ-Fe₂O₃/IF) can be obtained.

Structural characterizations

X-ray diffraction (XRD) was performed on a Philips X'Pert Pro Super diffractometer with Cu Kα radiation (λ = 1.54178 Å). The scanning electron microscopy (SEM) images were taken on a JEOL JSM-6700F SEM. The transmission electron microscopy (TEM) was carried out on a JEM-2100F field emission electron microscope at an acceleration voltage of 200 kV. The high-resolution TEM (HRTEM) was performed on a JEOL-2010 transmission electron microscope at an acceleration voltage of 200 kV. X-ray photoelectron spectroscopy (XPS) analyses were performed on a VGESCALAB MKII X-ray photoelectron spectrometer with an excitation source of Mg Kα = 1253.6 eV, and the resolution level was lower than 1 atom%. The inductively coupled plasma (ICP) emission spectrum was conducted on a Perkin Elmer Optima 7300DV ICP emission spectroscope.

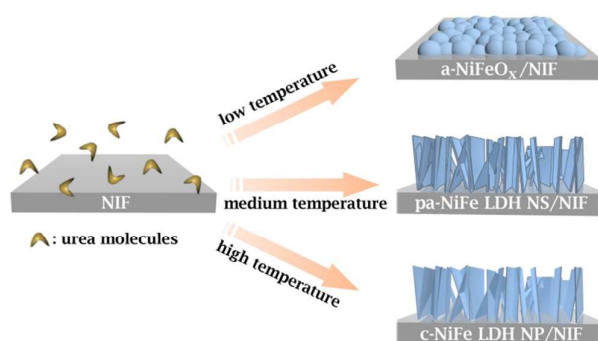
Electrocatalytic study

All the electrochemical measurements were performed in a three-electrode system linked with an electrochemical workstation (CHI660E) at room temperature. All potentials were calibrated to a reversible hydrogen electrode (RHE) and the data are presented without iR correction. In OER measurements, cyclic voltammetry (CV) and linear sweep

voltammetry (LSV) with a scan rate of 50 mV s^{-1} were conducted in 1 M KOH aqueous solution (pH=14, saturated with pure O_2). A Hg/HgO electrode was used as the reference electrode, a platinum gauze electrode ($2 \text{ cm} \times 2 \text{ cm}$, 60 mesh) was used as the counter electrode, and the treated foam electrode served as the working electrode which was fixed with an electrode holder. For the chronoamperometry test, a static overpotential of 370 mV (1.6 V vs. RHE) was applied. As for the UOR test, all operations were the same as above except that the electrolyte was replaced by the mixed solution containing 1 M KOH and 0.33 M urea. The electrochemical impedance spectroscopy (EIS) measurements were operated in the same configuration at open circuit voltage from 10^{-2} - 10^5 Hz. The impedance data were fitted to a simplified Randles circuit to extract the series and charge-transfer resistances.

Results and discussion

Structural and elemental characterizations



Scheme 1. Illustration of the formation processes of catalysts. Fully amorphous, partially amorphous and highly crystalline catalysts can be fabricated by tuning the synthesis temperature.

By serving NiFe alloy foam as both metal precursor and conductive substrate, partially amorphous nickel-iron layered double hydroxide nanosheet arrays grown on NiFe alloy foam (denoted as pa-NiFe LDH NS/NIF) were prepared, which can be used directly as a freestanding anode for water electrolysis (Scheme 1). During the formation process, urea molecules can offer a weak alkaline environment for the oxidation of metal substrate to form corresponding hydroxide, and the carbonate ions from the decomposition of urea can be simultaneously intercalated into hydroxide layers to form LDH structure. Of note, the crystallinity of products can be rationally modulated by simply varying the synthesis temperature. Fully amorphous NiFeO_x film on NiFe alloy foam (a-NiFeO_x/NIF) and highly crystalline NiFe LDH nanoplates on NiFe alloy foam (c-NiFe LDH NP/NIF) can be formed (Scheme 1, Fig. S1-2) at lower and higher temperatures, while at medium temperature (100°C), NiFe LDH nanosheet arrays with partially amorphous feature can be obtained. X-ray diffraction (XRD) technique was first conducted to investigate the structural information of the

obtained partially amorphous sample. As shown in Fig. 1A, besides the peaks originated from the alloy substrate, three sharp peaks located at 11.2° , 22.5° and 34.3° can be revealed with d spacings of 7.90 Å, 3.95 Å and 2.63 Å, corresponding to the (003), (006) and (009) reflections of NiFe LDH with preferential exposure of the basal planes. In addition, an extensively broadened peak in the range of 17° ~ 36° can be observed, which is characteristic for amorphous structure, therefore suggesting the partially amorphous nature of the product.^{29,30} In addition, by replacing the alloy foam to NiFe alloy foam with higher Fe content, pure Ni foam, and pure Fe foam, spinel NiFe₂O₄ nanoplates grown on NiFe foam (NiFe₂O₄ NP/NIF), Ni(OH)₂ nanosheets grown on nickel foam (Ni(OH)₂/NF) as well as γ -Fe₂O₃ grown on iron foam (γ -Fe₂O₃/IF) can be synthesized as counterparts with different Ni:Fe ratios (Fig. S3-4).

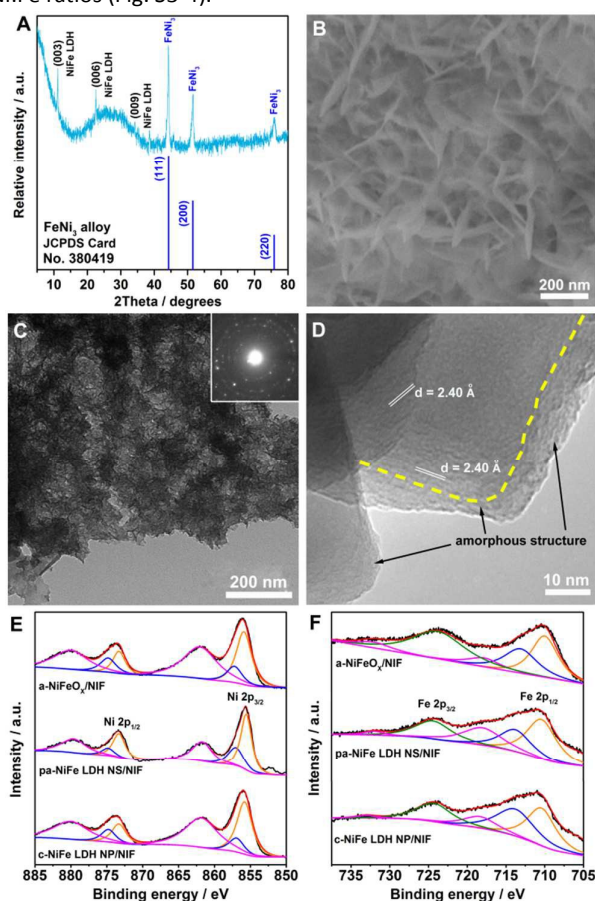


Fig. 1 (A) XRD pattern of pa-NiFe LDH NS/NIF. (B) SEM image of pa-NiFe LDH nanosheet arrays grown on the alloy foam. (C) TEM image of the pa-NiFe LDH nanosheets separated from the alloy foam. The inset shows SAED pattern. (D) HRTEM image of pa-NiFe LDH nanosheets indicates the co-existence of crystalline and amorphous structure. The crystalline-amorphous interface is labeled by yellow dash line. (E-F) XPS spectra of nickel and iron for a-NiFeO_x/NIF, pa-NiFe LDH NS/NIF and c-NiFe LDH NP/NIF.

ARTICLE

Journal Name

In order to further study the morphological information of pa-NiFe LDH NS/NIF, scanning electron microscopy (SEM) and transmission electron microscopy (TEM) were performed. As shown in Fig. 1B, well-defined ultrathin nanosheets can be observed with homogeneous lateral size of ~ 200 nm and thickness less than 10 nm. The thin layers may provide more reactive sites for the pre-oxidation of low-valence metal ions to electrochemically active high-valence species and thus benefit the electrooxidation behavior.³¹⁻³³ TEM image in Fig. 1C further confirms the ultrathin nanosheet morphology with hierarchical porous structure, which is beneficial for the diffusion of electrolyte as well as the gaseous or ionic products.^{34, 35} The selected area electron diffraction (SAED) pattern in the inset of Fig. 1C further demonstrates the partially amorphous feature of the product, where a relatively bright halo around the center spot can be identified, which can be considered as a solid evidence for the presence of amorphous species. Of note, considering the relatively low concentration of the amorphous species in the partially amorphous NiFe LDH nanosheet, the halo is not as bright as the typical fully amorphous material. In order to further understand the partially amorphous structure, high-resolution TEM (HRTEM) was carried out. As shown in Fig. 1D, interplanar spacing of 2.40 Å can be indexed, matching well with the (012) facets of NiFe LDH.³⁶ Of note, typical amorphous species with no crystal fringes can be revealed at the edge region of the nanosheets, therefore proving the partially amorphous structure of the as-grown nanosheets.

X-ray photoelectron spectroscopy (XPS) was performed to survey the composition and valence information of pa-NiFe LDH NS/NIF and its fully amorphous and highly crystalline counterparts. Since XPS technique is highly surface sensitive, the as-measured Ni:Fe atomic ratio of 5.75:1 can be regarded as the composition of partially amorphous NiFe LDH nanosheets. Of note, the Fe concentration of 14.8% is right in the range of broad maximum in OER activity according to previous reports,¹⁴ suggesting its high potential for OER. As can be seen from Fig. 1E, the Ni 2p spectrum of pa-NiFe LDH NS/NIF can be fitted as two spin-orbit doublets, characteristic of Ni²⁺ and Ni³⁺, and two shakeup satellites.^{37, 38} The binding energy of Ni 2p_{3/2} region can be deconvoluted into two peaks at 855.5 eV and 857.1 eV that match the oxidation states of Ni²⁺ and Ni³⁺, respectively; while the binding energy of Ni 2p_{1/2} region can be deconvoluted into two peaks centered at 873.3 eV and 874.7 eV, corresponding to Ni²⁺ and Ni³⁺, respectively.³⁷ Furthermore, two broad peaks at 861.8 eV and 879.8 eV can be indexed to the satellite peaks of 2p_{3/2} and 2p_{1/2} spin orbits, respectively. Therefore, the mixed valence of nickel can be confirmed, and the presence of native Ni³⁺ species may originate from the abundant crystalline/amorphous interfaces as well as the amorphous structure where the coordinating environment of nickel is strongly varied.³⁹ Similarly, native Ni³⁺ ions can also be detected for a-NiFeO_x/NIF owing to its fully amorphous structure with abundant low-coordinated Ni ions,

while the Ni³⁺ ions in c-NiFe LDH NP/NIF may arise from the higher synthesis temperature that endows a higher oxidation level of metal foam, which is crucial for the stabilization of LDH structure that requires proper M²⁺:M³⁺ ratio. Besides, the Fe 2p profile (Fig. 1F) located at 713.1 and 725.2 eV can be assigned to Fe 2p_{3/2} and Fe 2p_{1/2} for Fe³⁺ species, respectively.^{40, 41} The Fe 2p_{3/2} is accompanied by a satellite line at 718.3 eV, indicating the presence of Fe³⁺ ions.⁴² In addition, the peak at 714.1 eV implies that Fe³⁺ ions exist in more than one coordination environment, which could be attributed to the high affinity of neighboring Ni²⁺ ions.^{42, 43} Therefore, Ni_{5.75}Fe LDH with partially oxidized Ni³⁺ ions can be confirmed. The native Ni³⁺ ions may play a key role in stabilizing the LDH structure to achieve both optimal Fe concentration and M²⁺:M³⁺ ratio, and offer a potential in boosting the electrocatalytic oxidation reactions such as OER and UOR.

Electrochemical impedance spectroscopy and electrochemical double-layer capacitance

Electrochemical impedance spectroscopy (EIS) was performed to investigate the electrochemical kinetics and conductivity of different catalysts. As can be seen in Fig. 2A and Table 1, all catalysts display similar small series resistances of ~ 3 Ω at 0.9 V vs. RHE, which are benefited from the highly conductive metal foam skeleton. Of note, the much smaller radius of curvature for pa-NiFe LDH NS/NIF suggests the smaller charge transfer resistance (R_{ct}), which could be fitted to be 1236 Ω at a non-redox voltage of 0.9 V vs. RHE, much smaller than its counterparts. The smaller R_{ct} value may arise from the 2D conductive pathway along the vertically aligned ultrathin nanosheets.^{12, 44} Of note, the smaller R_{ct} value of the partially amorphous catalyst may boost the pre-oxidation process to reach a more facile generation of the catalytically active high-valence species, thereby lead to better performance for electrooxidation reactions.

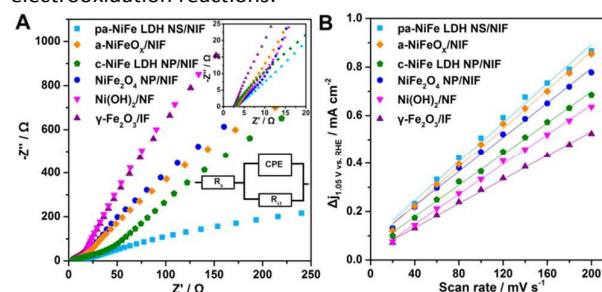


Fig. 2 (A) Nyquist plots of catalysts with different Ni:Fe ratios and crystallinity at 0.9 V vs. RHE. Inset shows the equivalent circuit. (B) The current density variation at a non-redox region plotted against scan rates to estimate C_{dl} .

Besides the conductivity issues, electrochemical surface area (ECSA) is another key parameter that strongly influences the electrocatalytic behaviors. Electrochemical double-layer capacitance (C_{dl}), which is linearly proportional to ECSA, is well-accepted to be an effective criterion to evaluate the ECSA of electrocatalysts.⁴⁴ As shown in Fig. 2B and Table 1, the C_{dl}

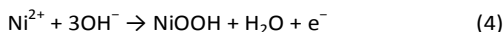
value of pa-NiFe LDH NS/NIF is calculated to be 2.2 mF cm^{-2} , which is similar to other counterparts with those values in the range of $1.23\text{-}1.98 \text{ mF cm}^{-2}$. The similarly high C_{dl} values arise from the highly porous metal foam skeleton with surface nanostructures that guarantees large surface area to adsorb ions in the electrolyte. Since C_{dl} is proportional to ECSA, the structural benefits of metal foam-based catalysts can be verified, which is advantageous to electrocatalytic processes such as OER and UOR.

Table 1 Comparison of series resistances, charge transfer resistances and electrochemical double-layer capacitances.

	R_s [Ω]	R_{ct} [Ω]	C_{dl} [mF cm^{-2}]
pa-NiFe LDH NS/NIF	2.9	1236	2.02
a-NiFeO _x /NIF	3.3	2235	1.98
c-NiFe LDH NP/NIF	2.9	2018	1.62
NiFe ₂ O ₄ NP/NIF	3.2	2875	1.78
Ni(OH) ₂ /NF	3.7	3326	1.55
γ -Fe ₂ O ₃ /IF	3.1	3020	1.23

Investigations on oxygen evolution reaction

In order to verify the influences of crystallinity and Ni:Fe ratio to the electrocatalytic behaviors, oxygen-evolving activity was firstly investigated for these freestanding electrodes in O₂-saturated 1 M KOH solution. As can be seen from the polarization curves in Fig. 3A, pa-NiFe LDH NS/NIF shows an earlier oxidation peak centered at $\sim 1.39 \text{ V}$ vs. RHE, corresponding to the electrochemical oxidation from divalent Ni ions to catalytically active Ni³⁺ species (equation 4). Of note, this oxidation peak is approximately 20-80 mV lower than those of Ni-containing counterparts, suggesting the easier electrooxidation of Ni²⁺ in pa-NiFe LDH NS/NIF. The possible reason for the negative shift in Ni²⁺-to-Ni³⁺ oxidation peak may arise from the partially amorphous structure which offers both electrochemically active low-coordinated Ni ions in amorphous area and facile charge transport guaranteed by the crystalline basal planes. Interestingly, the peak potential of pa-NiFe LDH NS/NIF matches well with the former result on highly porous β -Ni(OH)₂ nanomesh with rich coordinately unsaturated Ni ions, indicating the similar oxidation kinetics during positive sweep.⁴⁵ Besides, no oxidation peak can be observed for γ -Fe₂O₃/IF, which is consistent with previous reports for iron oxide based OER catalysts.⁴⁰ Accordingly, Tafel plots in Region 1 (Fig. 3B) corresponds to the Ni²⁺-to-Ni³⁺ oxidation process, and the fitted Tafel slopes of Ni-containing catalysts can be used to estimate the ease of occurrence for the following reaction:



Focused on the Ni²⁺-to-Ni³⁺ oxidation process in Region 1, the Tafel slope of pa-NiFe LDH NS/NIF is measured to be $38 \text{ mV decade}^{-1}$, which is smaller than the other Ni-containing counterparts with values in the range of $50\text{-}79 \text{ mV decade}^{-1}$ (Fig. 3B and Table 2), thus confirming the more facile reaction kinetics from catalytically inert Ni²⁺ species to active Ni³⁺ ions. The smaller Tafel slope of pa-NiFe LDH NS/NIF may arise from the abundant crystalline/amorphous interfaces that could

provide more reactive surface sites and fast charge transport. The easier oxidation can lead to faster generation of catalytically active Ni³⁺ species at a relatively low bias, thus accelerating the electrooxidation reactions such as OER and UOR. In addition, when applying potentials beyond the oxidation peak, the anodic current density of pa-NiFe LDH NS/NIF increases dramatically and achieves a 30 mA cm^{-2} current at an overpotential (η_{30}) of only 233 mV. While for other catalysts with various crystallinity and Ni:Fe ratio, much higher overpotentials of 273-505 mV are required to reach the same current density (Table 2), thus confirming the high OER activity of pa-NiFe LDH NS/NIF. Of note, this value ($\eta_{30}=233 \text{ mV}$) is smaller than that of the NiFe LDH/Ni foam from solution precursor ($\eta_{30}=280 \text{ mV}$), which may arise from the ultimate attachment between the in-situ formed NiFe LDH nanosheets and the alloy substrate.⁴⁶ Furthermore, to achieve a higher current of 100 mA cm^{-2} , pa-NiFe LDH NS/NIF only requires a low η_{100} of 326 mV, which is 40-201 mV lower than the other counterparts (Table 2), thus further demonstrating its high OER activity. Moreover, when applying higher overpotential, the OER activity of pa-NiFe LDH NS/NIF is even more predominant. For instance, at $\eta=500 \text{ mV}$, pa-NiFe LDH NS/NIF possesses a high anodic current density of 284.4 mA cm^{-2} , which shows 2.2-10.0 times enhancement than other catalysts with various Ni:Fe ratios. Of note, benefited from the highly exposed low-coordinated Ni ions, fully amorphous a-NiFeO_x/NIF also exhibits good OER activity with j_{geo} of 249.5 mA cm^{-2} at $\eta=500 \text{ mV}$, while its drawback in electrochemical stability will be discussed later. In addition, in order to investigate the intrinsic OER activity, the LSV curves were normalized with C_{dl} values to exclude the influence of surface area (Fig. S8). As listed in Table 2, the normalized current (j_{cat}) of pa-NiFe LDH NS/NIF at $\eta=300 \text{ mV}$ reaches 37.2 A F^{-1} , which is roughly 1.5-28.6 times larger than its counterparts. Besides, the identification of onset overpotential is difficult since the starting region of OER is overlapped by the oxidation peak, while considering the decreasing tail of this oxidation peak, the onset overpotential should be lower than 210 mV.⁴⁵ From the cathodic line of CV curve (Fig. S10A), the onset overpotential is estimated to be as low as 175 mV, confirming the superior activity of pa-NiFe LDH NS/NIF.⁴⁷ Same interferences can also be observed in corresponding Tafel plots. As shown in Fig. 3B and Table 2, the Tafel slopes in Region 2 of all Ni-containing catalysts are rather large, with value of $157 \text{ mV decade}^{-1}$ for pa-NiFe LDH NS/NIF and even larger for other Ni-containing counterparts ($176\text{-}445 \text{ mV decade}^{-1}$), which can be attributed to the severe interference of the Ni²⁺-to-Ni³⁺ oxidation peak to the OER onset region.⁴⁵ In sharp contrast, γ -Fe₂O₃/IF without such an ion oxidation process exhibits smaller Tafel slope of $107 \text{ mV decade}^{-1}$. In order to exclude this interference, Tafel curve from the cathodic sweep of CV curve was plotted,⁴⁷ from which a much smaller Tafel slope of $63 \text{ mV decade}^{-1}$ can be identified for pa-NiFe LDH NS/NIF (Fig. S10B), thus confirming its facile OER kinetics.

Table 2 Comparison of electrochemical parameters of OER.

	$\eta_{30\text{mA cm}^{-2}}$ [mV]	$\eta_{100\text{mA cm}^{-2}}$ [mV]	j_{geo} ($\eta=500$ mV) [mA cm ⁻²]	j_{cdl} ($\eta=300$ mV) [A F ⁻¹]	Tafel slope (Region1) [mV decade ⁻¹]	Tafel slope (Region2) [mV decade ⁻¹]
pa-NiFe LDH NS/NIF	233	326	284.4	37.2	38	157
a-NiFeO _x /NIF	283	366	249.5	20.3	64	176
c-NiFe LDH NP/NIF	273	406	160.8	24.5	79	178
NiFe ₂ O ₄ NP/NIF	307	453	128.9	14.9	50	197
Ni(OH) ₂ /NF	505	-	28.6	11.6	57	445
γ -Fe ₂ O ₃ /IF	443	527	75.1	1.3	-	107

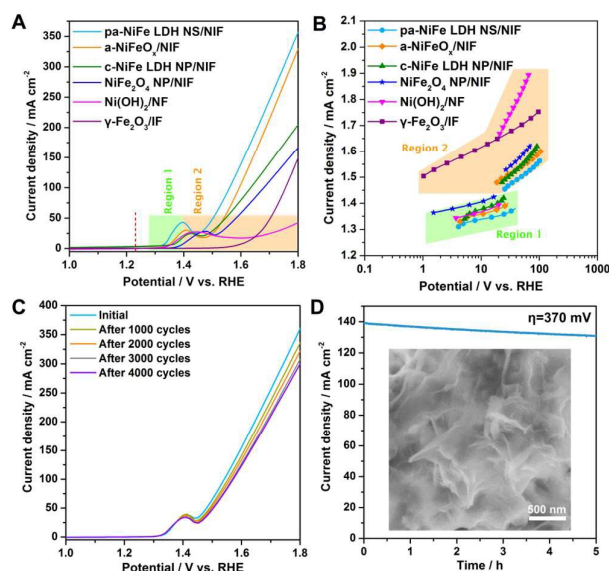


Fig. 3 (A) Linear sweep voltammetry (LSV) curves measured in 1 M KOH solution. (B) Corresponding Tafel plots of various catalysts. The light green shadow highlights the Tafel region for Ni²⁺-to-Ni³⁺ oxidation, while the Tafel curves in the orange region represent a combined process of OER and Ni²⁺-to-Ni³⁺ oxidation (γ -Fe₂O₃/IF for OER only). (C) Stability test of pa-NiFe LDH NS/NIF for long-term CV cycling. (D) Chronoamperometry data of pa-NiFe LDH NS/NIF obtained in 1 M KOH solution at an overpotential of 370 mV. The inset shows the SEM image after OER chronoamperometry test.

Apart from the OER activity, the electrochemical stability is also important to evaluate an advanced electrocatalyst, especially for practical applications. Long-term cyclic voltammetry (CV) and chronoamperometry were performed to describe the stability of pa-NiFe LDH NS/NIF. As shown in Fig.

3C, slight degradation of current density can be revealed during CV cycling, and as the cycling proceeds, the current decreased at a slower rate, for instance, the curves after 3000 and 4000 cycles are almost unchanged. After 4000 CV cycles, a large OER current of 239 mA cm⁻² can still be obtained at $\eta=500$ mV, indicating the high activity during long-term CV cycling. The operational stability was further evaluated by chronoamperometry test under fixed overpotential. As shown in Fig. 3D, the current density at $\eta=370$ mV only shows a slight degradation of ~5.3% after 5-hour continuous OER operation. The current retention of 94.7% of partially amorphous catalyst is similar to that of the highly crystalline sample (93.8%) and much higher than the fully amorphous catalyst (73.5%) which is considered to be relatively soluble under continuous operation (Fig. S11).⁴⁸⁻⁵⁰ Furthermore, as confirmed by SEM image, the nanosheet morphology is retained after long-term OER operation (inset of Fig. 3D), while the XPS analyses of the pa-NiFe LDH NS/NIF catalyst after 10 h continuous OER operation indicate that the proportion of high-valence Ni and Fe species increases compared with the fresh catalyst (Fig. S12), which can be attributed to the surface activation of the catalyst.

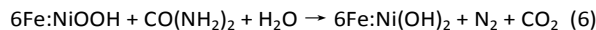
Investigations on urea oxidation reaction

Beyond OER, electrocatalytic urea oxidation reaction is also of great importance as a combined process to synergistically achieve both energy conversion and waste water treatment. According to previous report, the UOR process (equation 2) is a combined process that involves an electrochemical oxidation step (equation 5) and a chemical redox step (equation 6),⁵¹ as shown below:

Electrochemical process:



Chemical process:



where the NiFe LDH is denoted as Fe:Ni(OH)₂, and Fe:NiOOH represents its high-valence state after electrooxidation. As demonstrated in previous research, the UOR process can be divided into two individual steps, that is, i) electrochemical oxidation process of Ni-containing catalyst to generate high-valence phase; and ii) chemical oxidation of urea molecules on surface of as-generated high-valence oxidative catalyst. Herein, the native Ni³⁺ ions in the partially amorphous nanosheet may trigger UOR process at a lower bias, and the amorphous edges with low-coordinated Ni ions can be easily oxidized into high-valence phases and thus further improving the UOR activity. In order to achieve a good UOR performance, LSV curves were measured in 1 M KOH solution containing various urea concentration for pa-NiFe LDH NS/NIF. As can be seen from Fig. S13, the optimal urea concentration to achieve a higher UOR current can be determined to be 0.33 M, which is similar to the result in a recent work on α-Ni(OH)₂/NF UOR catalyst.⁵² That is, at lower urea concentrations below 0.33 M, the UOR current increases which can be attributed to the diffusion-controlled reaction mechanism, while at concentrations higher than 0.33 M, the UOR current decreases since most active sites on the surface of Fe:NiOOH are covered with urea and its oxidation intermediate molecules which in turn decreases the oxidation rate of urea owing to the local deprivation of OH⁻ species.^{8, 52}

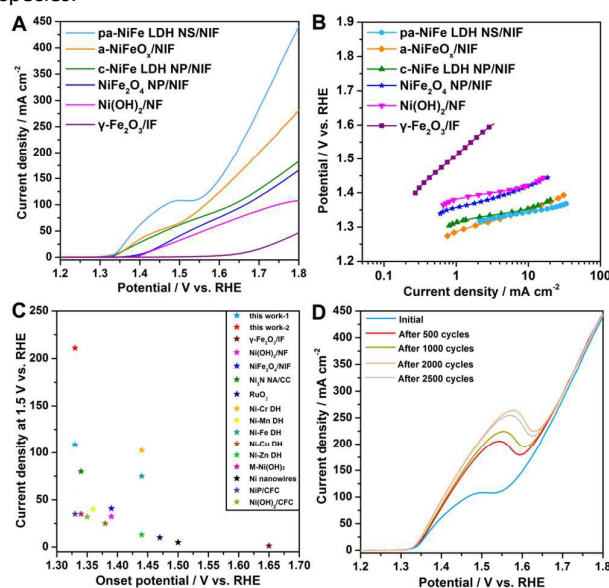


Fig. 4 (A) UOR curves of various catalysts in 1 M KOH with 0.33 M urea. (B) Corresponding Tafel plots. (C) Comparison of UOR activity of various catalysts measured in 1 M KOH and 0.33 M urea. The samples "this work-1/2" represent the fresh and activated (after 2000 CV cycles) pa-NiFe LDH NS/NIF catalysts, respectively. (D) An activation process can be revealed along with CV cycling test.

By using the optimized electrolyte with 1 M KOH and 0.33 M urea, UOR curves of various catalysts can be obtained. As shown in Fig. 4A-B, pa-NiFe LDH NS/NIF demonstrates excellent performance with a high UOR catalytic activity and favorable reaction kinetics. The UOR onset potential can be identified to be 1.322 V vs. RHE, which is close to the onset of the Ni²⁺-to-Ni³⁺ oxidation in OER curve (Fig. S14). The early UOR onset may arise from the native Ni³⁺ active sites that can trigger UOR at a relatively low bias. Besides, geometric current density is another key parameter to evaluate the UOR activity. As shown in Fig. 4A and Table 3, to reach a 30 mA cm⁻² current, pa-NiFe LDH NS/NIF only requires a low bias of 1.362 V vs. RHE, which is 30 mV and 43 mV lower than the fully amorphous and highly crystalline catalysts with the same Ni:Fe ratio. When compared with the catalysts with different Ni:Fe ratios, the UOR activity of pa-NiFe LDH NS/NIF is more prominent (Table 3), and much higher potentials of 1.471-1.749 mV vs. RHE are needed to reach the same current density. In addition, this superiority is even larger when pursuing a higher current. For instance, an applied potential of 1.459 V vs. RHE can lead to a high current density of 100 mA cm⁻² for pa-NiFe LDH NS/NIF, while for fully amorphous and highly crystalline ones, 106 mV and 174 mV higher potentials are required, respectively. Besides, at an applied potential of 1.8 V vs. RHE, pa-NiFe LDH NS/NIF with partially amorphous feature shows a much larger UOR current of 440.6 mA cm⁻², which is roughly 1.6 and 2.4 times larger than the fully amorphous and highly crystalline catalysts, and 2.7-9.4 folds larger than the catalysts with other Ni:Fe ratios. The enhanced UOR activity of pa-NiFe LDH NS/NIF may arise from the easier generation of high-valence species as well as the native Ni³⁺ ions that can facilitate the electrochemical adsorption of urea molecules and subsequent raise the UOR rate. Similar to OER analysis, UOR currents normalized by C_{dl} were also provided to eliminate the influence brought by variable ECSA. As shown in Fig. S15 and Table 3, when applying a bias of 1.8 V vs. RHE, a high normalized current of 221.2 A F⁻¹ can be obtained for pa-NiFe LDH NS/NIF, which is much larger than the other catalysts (35.8-139.3 A F⁻¹) with either different crystallinity or Ni:Fe ratio, therefore confirming the high activity in UOR catalysis. The facile reaction kinetics can be further verified by analyzing the corresponding Tafel plots. As shown in Fig. 4B and Table 3, pa-NiFe LDH NS/NIF demonstrates the smallest Tafel slope of 33 mV decade⁻¹, which can be attributed to its nanosheet array morphology with good in-plane conductivity and rich active sites. c-NiFe LDH NP/NIF and Ni(OH)₂/NF with similar morphology also show relatively low Tafel slope of 39 and 38 mV decade⁻¹, respectively, while in this case the low density of active sites restricts their UOR activity. For the other counterparts with poor crystallinity or non-sheet surface morphology, the Tafel slopes are much larger, thus severely restricting their UOR behavior. A comparison of UOR activity between pa-NiFe LDH NS/NIF catalysts and other as-explored UOR catalysts is summarized in Fig. 4C,⁵³⁻⁵⁷ from which the

dominance of UOR activity in both onset overpotential and current density under fixed potential can be clearly identified.

Long-term CV measurement was conducted to further evaluate the electrochemical stability of pa-NiFe LDH NS/NIF in UOR catalysis. As shown in Fig. 4D, an obvious activation process can be revealed during the first 2000 CV cycles, where the peak current shows remarkable increment from 109.8 mA cm⁻² for the initial cycle to 264.5 mA cm⁻² for the 2000th cycle. Beyond 2000 CV cycles, the peak current only shows slight degradation to 256.2 mA cm⁻² after 2500 CV cycles, demonstrating good activity and stability for long-term UOR

operation. The beneficial activation effect can be further confirmed by the variation of required potentials to achieve a UOR current density of 100 mA cm⁻². For the fresh pa-NiFe LDH NS/NIF catalyst, a potential of 1.459 V vs. RHE is required, while along with the CV-induced activation, the demanded bias decreases obviously and finally can be stabilized to 1.404 V vs. RHE after 2000 CV cycles. Furthermore, no current degradation appears at higher potentials, *i.e.* 1.8 V vs. RHE even after 2500 CV cycles, further confirming the excellent electrochemical stability of the partially amorphous freestanding catalyst.

Table 3 Comparison of electrochemical parameters of UOR.

	Required potential for 30 mA cm ⁻² [mV vs. RHE]	Required potential for 100 mA cm ⁻² [mV vs. RHE]	j_{geo} @1.8 V vs. RHE [mA cm ⁻²]	j_{cd} @1.8 V vs. RHE [A F ⁻¹]	Tafel slope (UOR) [mV decade ⁻¹]
pa-NiFe LDH NS/NIF	1.362	1.459	440.6	221.2	33
a-NiFeO _x /NIF	1.392	1.565	281.0	139.3	67
c-NiFe LDH NP/NIF	1.405	1.633	183.2	111.8	39
NiFe ₂ O ₄ NP/NIF	1.471	1.664	164.3	91.8	61
Ni(OH) ₂ /NF	1.492	1.744	108.0	69.1	38
γ-Fe ₂ O ₃ /IF	1.749	—	46.9	35.8	184

Conclusions

In summary, partially amorphous NiFe LDH nanosheet arrays with native Ni³⁺ ions and optimal Ni:Fe ratio were developed, realizing robust performance on both electrocatalytic oxygen evolution and urea oxidation. The partially amorphous structure can not only bring in native Ni³⁺ ions and lead to facile generation of high-valence active species for these electrooxidation reactions, but also offer 2D charge transfer pathway to facilitate the electrocatalytic process. Besides, the optimized Ni:Fe ratio as well as the large active surface area further enhance the catalytic activity, and the partially amorphous structure guarantees high stability towards long-term operation. This work may enrich the design strategy of electrocatalysts for both water electrolysis and electrooxidation of energy-containing small molecules, as well as provide a robust bifunctional electrooxidation catalyst for simultaneous waste water treatment and clean energy production.

Conflicts of interest

There are no conflicts to declare.

Acknowledgements

This work was supported by the National Natural Science Foundation of China (21501112, 21390411, 21701102, 21535004 and 91753111) and the Natural Science Foundation of Shandong Province (ZR2018JL009).

References

- M. S. Dresselhaus and I. L. Thomas, *Nature*, 2001, **414**, 332-337.
- T. E. Mallouk, *Nature Chem.*, 2013, **5**, 362-363.
- Z. W. Seh, J. Kibsgaard, C. F. Dickens, I. Chorkendorff, J. K. Nørskov and T. F. Jaramillo, *Science*, 2017, **355**, eaad4998.
- E. Fabbri, A. Habereder, K. Waltar, R. Kotz and T. J. Schmidt, *Catal. Sci. Technol.*, 2014, **4**, 3800-3821.
- H. Jin, C. Guo, X. Liu, J. Liu, A. Vasileff, Y. Jiao, Y. Zheng and S.-Z. Qiao, *Chem. Rev.*, 2018, DOI: 10.1021/acs.chemrev.7b00689.
- R. P. Forslund, J. T. Mefford, W. G. Hardin, C. T. Alexander, K. P. Johnston and K. J. Stevenson, *ACS Catal.*, 2016, **6**, 5044-5051.
- R. Ding, L. Qi, M. Jia and H. Wang, *Nanoscale*, 2014, **6**, 1369-1376.
- V. Vedharathinam and G. G. Botte, *Electrochim. Acta*, 2012, **81**, 292-300.
- M. Liu, L. Yang, T. Liu, Y. Tang, S. Luo, C. Liu and Y. Zeng, *J. Mater. Chem. A*, 2017, **5**, 8608-8615.
- B. K. Boggs, R. L. King and G. G. Botte, *Chem. Commun.*, 2009, **0**, 4859-4861.
- J. Xie and Y. Xie, *ChemCatChem*, 2015, **7**, 2568-2580.
- Y. Tong, P. Chen, M. Zhang, T. Zhou, L. Zhang, W. Chu, C. Wu and Y. Xie, *ACS Catal.*, 2018, **8**, 1-7.
- J. Xie and Y. Xie, *Chem. Eur. J.*, 2016, **22**, 3588-3598.
- F. Dionigi and P. Strasser, *Adv. Energy Mater.*, 2016, **6**, 1600621.
- A. S. Batchellor and S. W. Boettcher, *ACS Catal.*, 2015, **5**, 6680-6689.
- O. Diaz-Morales, I. Ledezma-Yanez, M. T. M. Koper and F. Calle-Vallejo, *ACS Catal.*, 2015, **5**, 5380-5387.
- T. T. H. Hoang and A. A. Gewirth, *ACS Catal.*, 2016, **6**, 1159-1164.

18. M. W. Louie and A. T. Bell, *J. Am. Chem. Soc.*, 2013, **135**, 12329-12337.
19. M. Gong and H. Dai, *Nano Res.*, 2015, **8**, 23-39.
20. Z. Lu, W. Xu, W. Zhu, Q. Yang, X. Lei, J. Liu, Y. Li, X. Sun and X. Duan, *Chem. Commun.*, 2014, **50**, 6479-6482.
21. S. Jin, *ACS Energy Lett.*, 2017, **2**, 1937-1938.
22. L. Trotochaud, J. K. Ranney, K. N. Williams and S. W. Boettcher, *J. Am. Chem. Soc.*, 2012, **134**, 17253-17261.
23. H.-Y. Wang, Y.-Y. Hsu, R. Chen, T.-S. Chan, H. M. Chen and B. Liu, *Adv. Energy Mater.*, 2015, **5**, 1500091.
24. F. Hu, S. Zhu, S. Chen, Y. Li, L. Ma, T. Wu, Y. Zhang, C. Wang, C. Liu, X. Yang, L. Song, X. Yang and Y. Xiong, *Adv. Mater.*, 2017, **29**, 1606570.
25. H. Liang, A. N. Gandi, C. Xia, M. N. Hedhili, D. H. Anjum, U. Schwingenschlöggl and H. N. Alshareef, *ACS Energy Lett.*, 2017, **2**, 1035-1042.
26. J. Zhang, Y. Hu, D. Liu, Y. Yu and B. Zhang, *Adv. Sci.*, 2017, **4**, 1600343.
27. R. D. L. Smith, M. S. Prévot, R. D. Fagan, Z. Zhang, P. A. Sedach, M. K. J. Siu, S. Trudel and C. P. Berlinguette, *Science*, 2013, **340**, 60-63.
28. L. Kuai, J. Geng, C. Chen, E. Kan, Y. Liu, Q. Wang and B. Geng, *Angew. Chem. Int. Ed.*, 2014, **53**, 7547-7551.
29. Y. Idota, T. Kubota, A. Matsufuji, Y. Maekawa and T. Miyasaka, *Science*, 1997, **276**, 1395-1397.
30. B. Zhang, X. Zheng, O. Voznyy, R. Comin, M. Bajdich, M. García-Melchor, L. Han, J. Xu, M. Liu, L. Zheng, F. P. García de Arquer, C. T. Dinh, F. Fan, M. Yuan, E. Yassitepe, N. Chen, T. Regier, P. Liu, Y. Li, P. De Luna, A. Janmohamed, H. L. Xin, H. Yang, A. Vojvodic and E. H. Sargent, *Science*, 2016, **352**, 333-337.
31. Y. Sun, S. Gao, F. Lei and Y. Xie, *Chem. Soc. Rev.*, 2015, **44**, 623-636.
32. W. Yang, X. Zhang and Y. Xie, *Nano Today*, 2016, **11**, 793-816.
33. Y. Dou, L. Zhang, X. Xu, Z. Sun, T. Liao and S. X. Dou, *Chem. Soc. Rev.*, 2017, **46**, 7338-7373.
34. J. Xie, J. Xin, G. Cui, X. Zhang, L. Zhou, Y. Wang, W. Liu, C. Wang, M. Ning, X. Xia, Y. Zhao and B. Tang, *Inorg. Chem. Front.*, 2016, **3**, 1160-1166.
35. J. Xie, H. Qu, J. Xin, X. Zhang, G. Cui, X. Zhang, J. Bao, B. Tang and Y. Xie, *Nano Res.*, 2017, **10**, 1178-1188.
36. M. Gong, Y. Li, H. Wang, Y. Liang, J. Z. Wu, J. Zhou, J. Wang, T. Regier, F. Wei and H. Dai, *J. Am. Chem. Soc.*, 2013, **135**, 8452-8455.
37. C. Shang, S. Dong, S. Wang, D. Xiao, P. Han, X. Wang, L. Gu and G. Cui, *ACS Nano*, 2013, **7**, 5430-5436.
38. Z. Zhao, H. Wu, H. He, X. Xu and Y. Jin, *Adv. Funct. Mater.*, 2014, **24**, 4698-4705.
39. Y. Zhao, X. Jia, G. Chen, L. Shang, G. I. N. Waterhouse, L.-Z. Wu, C.-H. Tung, D. O'Hare and T. Zhang, *J. Am. Chem. Soc.*, 2016, **138**, 6517-6524.
40. J. Xie, W. Liu, J. Xin, F. Lei, L. Gao, H. Qu, X. Zhang and Y. Xie, *ChemSusChem*, 2017, **10**, 4465-4471.
41. C. Dong, T. Kou, H. Gao, Z. Peng and Z. Zhang, *Adv. Energy Mater.*, 2017, **8**, 1701347.
42. Y. Liu, J. Li, F. Li, W. Li, H. Yang, X. Zhang, Y. Liu and J. Ma, *J. Mater. Chem. A*, 2016, **4**, 4472-4478.
43. Z. Gu, X. Xiang, G. Fan and F. Li, *J. Phys. Chem. C*, 2008, **112**, 18459-18466.
44. J. Xie, J. Zhang, S. Li, F. Grote, X. Zhang, H. Zhang, R. Wang, Y. Lei, B. Pan and Y. Xie, *J. Am. Chem. Soc.*, 2013, **135**, 17881-17888.
45. J. Xie, X. Zhang, H. Zhang, J. Zhang, S. Li, R. Wang, B. Pan and Y. Xie, *Adv. Mater.*, 2017, **29**, 1604765.
46. Z. Lu, W. Xu, W. Zhu, Q. Yang, X. Lei, J. Liu, Y. Li, X. Sun and X. Duan, *Chem. Commun.*, 2014, **50**, 6479-6482.
47. K. Xu, H. Ding, K. Jia, X. Lu, P. Chen, T. Zhou, H. Cheng, S. Liu, C. Wu and Y. Xie, *Angew. Chem. Int. Ed.*, 2016, **55**, 1710-1713.
48. J. D. Benck, Z. Chen, L. Y. Kuritzky, A. J. Forman and T. F. Jaramillo, *ACS Catal.*, 2012, **2**, 1916-1923.
49. J. Xie, H. Zhang, S. Li, R. Wang, X. Sun, M. Zhou, J. Zhou, X. W. Lou and Y. Xie, *Adv. Mater.*, 2013, **25**, 5807-5813.
50. A. B. Laursen, P. C. K. Vesborg and I. Chorkendorff, *Chem. Commun.*, 2013, **49**, 4965-4967.
51. V. Vedharathinam and G. G. Botte, *Electrochim. Acta*, 2013, **108**, 660-665.
52. M. A. Ghanem, A. M. Al-Mayouf, J. P. Singh and P. Arunachalam, *Electrocatalysis*, 2017, **8**, 16-26.
53. X. Zhu, X. Dou, J. Dai, X. An, Y. Guo, L. Zhang, S. Tao, J. Zhao, W. Chu, X. C. Zeng, C. Wu and Y. Xie, *Angew. Chem. Int. Ed.*, 2016, **55**, 12465-12469.
54. W. Yan, D. Wang, L. A. Diaz and G. G. Botte, *Electrochim. Acta*, 2014, **134**, 266-271.
55. X. Zhang, Y. Liu, Q. Xiong, G. Liu, C. Zhao, G. Wang, Y. Zhang, H. Zhang and H. Zhao, *Electrochim. Acta*, 2017, **254**, 44-49.
56. Q. Liu, L. Xie, F. Qu, Z. Liu, G. Du, A. M. Asiri and X. Sun, *Inorg. Chem. Front.*, 2017, **4**, 1120-1124.
57. W. Xu, D. Du, R. Lan, J. Humphreys, Z. Wu and S. Tao, *New J. Chem.*, 2017, **41**, 4190-4196.

Graphical Abstract

